JOURNAL OF GEOPHYSICAL RESEARCH, VOL. 113, A06102, doi:10.1029/2007JA012758, 2008

Implications of solar wind suprathermal tails for IBEX ENA images of the heliosheath

C. Prested,[1] N. Schwadron,[1] J. Passuite,[1] B. Randol,[1,2] B. Stuart,[1,3] G. Crew,[1,4] J. Heerikhuisen,[5] N. Pogorelov,[5] G. Zank,[5] M. Opher,[6] F. Allegrini,[2] D. J. McComas,[2] M. Reno,[2] E. Roelof,[7] S. Fuselier,[8] H. Funsten,[9] E. Moebius,[10] and L. Saul[11]

Received 24 August 2007; revised 1 February 2008; accepted 25 February 2008; published 12 June 2008.

[1] Decades of interplanetary measurements of the solar wind and other space plasmas have established that the suprathermal ion intensity distributions (j) are non-Maxwellian and are characterized by high-energy power law tails ($j \sim E^{-\kappa}$). Recent analysis by Fisk and Gloeckler of suprathermal ion observations between 1–5 AU demonstrates that a particular differential intensity distribution function emerges universally between ~2–10 times the solar wind speed with $\kappa \sim 1.5$. This power law tail is particularly apparent in downstream distributions beyond reverse shocks associated with corotating interaction regions. Similar power law tails have been observed in the downstream flow beyond the termination shock by the *Low Energy Charged Particle* instrument on both Voyager 1 and Voyager 2. Using kappa distributions with internal energy, density, and bulk flow derived from large-scale magnetohydrodynamic models, we calculate the simulated flux of energetic neutral atoms (ENAs) produced in the heliosheath by charge exchange between solar wind protons and interstellar hydrogen. We then produce simulated ENA maps of the heliosheath, such as will be measured by the Interstellar Boundary Explorer Mission (IBEX). We also estimate the expected signal to noise and background ratio for IBEX. The solar wind suprathermal tail significantly increases the ENA flux within the IBEX energy range, ~0.01–6 keV, by more than an order of magnitude at the highest energies over the estimates using a Maxwellian. It is therefore essential to consider suprathermal tails in the interpretation of IBEX ENA images and theoretical modeling of the heliospheric termination shock.

Citation: Prested, C., et al. (2008), Implications of solar wind suprathermal tails for IBEX ENA images of the heliosheath, *J. Geophys. Res.*, *113*, A06102, doi:10.1029/2007JA012758.

1. Introduction

[2] The Interstellar Boundary Explorer (IBEX), scheduled for launch in 2008, is designed to make the first global images of the heliosheath beyond the heliospheric termination shock, using energetic neutral atoms (ENAs) generated by charge exchange between downstream protons and interstellar hydrogen atoms [*McComas et al.*, 2004, 2006]. These ENAs are no longer bound to the magnetic field and therefore follow trajectories determined only by the gravitational force and radiation pressure from the Sun. A subset of these neutrals will reach IBEX in orbit around Earth at 1 AU, providing information about the outer edge of our solar system.

[3] This ENA emission is highly sensitive to the energy spectrum of the shocked solar wind. The spectrum can be divided into three parts: the Maxwellian-like distribution of the thermal core, the broad distribution of pickup ions extending up to twice the upstream solar wind speed, and the power law distribution of the suprathermal tail. Previous studies of heliospheric ENAs [e.g., *Gruntman et al.*, 2001] approximated the downstream ions as a Maxwellian core, a

[1]Department of Astronomy, Center for Space Physics and Center for Integrated Space Weather Modeling, Boston University, Boston, Massachusetts, USA.
[2]Space Science and Engineering Division, Southwest Research Institute, San Antonio, Texas, USA.
[3]Institute for Astronomy, University of Hawaii, Honolulu, Hawaii, USA.
[4]Kavli Institute for Astrophysics and Space Research, Massachusetts Institute for Technology, Cambridge, Massachusetts, USA.
[5]Institute of Geophysics and Planetary Physics, University of California, Riverside, California, USA.
[6]Department of Physics and Astronomy, George Mason University, Fairfax, Virginia, USA.
[7]Applied Physics Laboratory, Johns Hopkins University, Laurel, Maryland, USA.
[8]Space Physics Laboratory, Lockheed Martin, Palo Alto, California, USA.
[9]Los Alamos National Laboratory, Los Alamos, New Mexico, USA.
[10]Space Science Center and Department of Physics, University of New Hampshire, Durham, New Hampshire, USA.
[11]Physikalisches Institut, Space and Planetary Sciences, University of Bern, Bern, Switzerland.

0148-0227/08/2007JA012758$09.00

Maxwellian core plus a spherical distribution of pickup ions, or a Maxwellian core plus a Maxwellian distribution of pickup ions. Prior to this paper, to our knowledge no ENA flux calculation has included a power law tail. That is the purpose of this paper.

[4] Recently, the Voyager 1 and 2 *Low Energy Charged Particle* (*LECP*) detectors have established that a power law describes the heliosheath ions downstream of the termination shock in the energy range of ~30 keV to 10 MeV [*Decker et al.*, 2005; R. B. Decker et al., Voyager 2 encounter with an energetic-particle-mediated termination shock, submitted to *Science*, 2008]. Below 30 keV there is an unmeasured energy region, including the ~0.01–6 keV that will be investigated by IBEX. Consequently, it is not known where exactly in the energy spectrum the power law tail begins in the heliosheath. Taking into account the slowing of the solar wind by pickup ion accumulation [e.g., *Fisk*, 1996; *Isenberg*, 1997], adiabatic cooling, shock jump conditions, and empirical results, this break should occur at or below the energy at which it is observed in the average upstream solar wind ($\leq$1 keV). Therefore the suprathermal tail should populate a significant portion of the IBEX energy range.

[5] In preparation for the 2008 launch of IBEX, we take an ad hoc approach to simulating ENA images. We use the bulk parameters of the solar wind generated by two different magnetohydrodynamic (MHD) models of the heliosheath, and then apply the MHD moments (density, bulk velocity, and temperature) to distribution functions describing the thermal core and power law tail. One model (OSLG) is by *Opher et al.* [2006, 2007], and the other MHD model (PZO) is by *Pogorelov et al.* [2006]. We also produce simulated IBEX hydrogen ENA images and examine the expected noise and background sources.

2. Background

[6] The kappa distribution provides a single functional description of a thermal core and power law tail.

$$F(v) = \frac{n\Gamma(\kappa+1)}{w_o^3\pi^{3/2}\kappa^{3/2}\Gamma(\kappa-1/2)}\left[1+\frac{(|v-v_{SW}|)^2}{\kappa w_o^2}\right]^{-\kappa-1} \quad \text{where } w_o = \sqrt{\frac{2T}{m_p}\frac{(\kappa-3/2)}{\kappa}} \qquad (1)$$

Here $\boldsymbol{v}$ is the observed ion velocity and the solar wind bulk parameters are: number density n, bulk flow velocity $\boldsymbol{v}_{sw}$, and temperature T defined in the limit $\kappa \rightarrow \infty$. The empirical functional form of equation (1) was first proposed by *Vasyliunas* [1968] and is described here using the notation of *Collier* [1995]. It reduces to a Maxwellian distribution as κ, which describes the steepness of the power law tail, approaches ∞. Note, however, that the kappa function does not describe the intermediate "plateau" of pickup ions ($v < v_{SW}$ in the solar wind frame). The function is positive and continuous for all values $\boldsymbol{v}$ and tends toward 0 for large velocity values, satisfying the derivation requirements of ideal MHD from fluid dynamics, as found in a standard text [e.g., *Goossens*, 2003]. This functional form is further developed by *Summers and Thorne* [1991], who define the relevant plasma dispersion function, and by *Treumann et al.* [1999, 2004], who establish the thermodynamic foundation.

[7] The kappa distribution function has been used successfully to describe solar wind ions. *Collier et al.* [1996] fit kappa distributions to both fast and slow solar wind using WIND data. Also using WIND data, *Chotoo et al.* [2000] analyzed power law tails associated with corotating interaction regions and extracted the values of κ. The 2004 Voyager 1 termination shock crossing extends suprathermal tail observations into the heliosheath. The Voyager 1 *LECP* instrument observed a $\kappa = 1.6$ power law tail for hydrogen ions at $v \gg v_{sw}$ [*Decker et al.*, 2005]. While the acceleration mechanism for the power law tail is under debate, the diversity of regimes in which it has been observed indicates that it is a universal characteristic of plasma throughout the heliosphere and heliosheath.

[8] The Ulysses and ACE *Solar Wind Ion Composition Spectrometers* (SWICS) [*Gloeckler*, 1992] measured suprathermal tails at distances ranging from 1 AU to 5.4 AU, including in the quiet time solar wind [*Gloeckler*, 2003]. On the basis of these observations, *Fisk and Gloeckler* [2006] argued that there is a universal $\kappa \sim 1.5$ suprathermal tail of hydrogen ions which persists throughout the solar wind above 2 to 3 times v_{sw} (~1 keV). In practice the energy range and resolution has a significant influence on the functional fit.

3. Method

[9] The modeled hydrogen ENA fluxes and their simulated IBEX images are created using the OSLG and PZO models of the heliosheath. The PZO model includes a neutral hydrogen density profile, but for the OSLG model we assume the neutral hydrogen population throughout the heliosphere has the undisturbed density value, 0.1 cm^{-3} [e.g., *Pogorelov et al.*, 2006]. We extract plasma density, temperature, and bulk flow velocity of the downstream solar wind from the models and produce hydrogen ion distributions using both the kappa (equation (1)) and Maxwellian distribution. For the remainder of this paper we take $\kappa = 1.6$ for the downstream solar wind, based on the in situ measurement by Voyager 1, which is in good agreement with the Fisk and Gloeckler solar wind value of $\kappa \sim 1.5$. The ENA flux is determined through an appropriate integration, as defined below, over the distribution function of protons at various positions along the observer's line-of-sight. This ad hoc procedure is not theoretically self-consistent for the PZO case, because the model uses a Maxwellian distribution for ions and neutrals in calculating momentum and energy transfer due to charge exchange in the heliosheath. Still, it is useful to examine the impact of a kappa distribution on the PZO ENA flux.

[10] Since the observer is near 1 AU (and a line-of-sight extends far beyond 1 AU), we make the approximations that the observer is at a fixed origin and that the lines-of-sight extend along radial trajectories from the origin through the heliosphere. We assume ENAs travel in straight lines (the rectilinear approximation), although inside the termination shock ($r \lesssim 100$AU) the forces of solar gravitation and radiation pressure on hydrogen atoms are not negligible at

Table 1. Preliminary IBEX Energy Channels and Hydrogen Geometric Factors

Energy Channel	Central Energy, keV	Geometric Factor, 10^{-3} cm^2 sr eV/eV
Lo, 1	0.015	0.62
Lo, 2	0.029	1.0
Lo, 3	0.056	1.4
Lo, 4	0.107	1.7
Lo, 5	0.208	1.6
Lo, 6	0.403	1.5
Lo, 7	0.781	1.3
Lo, 8	1.515	1.0
Hi, 1	0.45	2.0
Hi, 2	0.71	3.4
Hi, 3	1.11	6.0
Hi, 4	1.74	7.5
Hi, 5	2.73	9.4
Hi, 6	4.29	13

low energies ($\ll$1 keV). These solar effects dwindle rapidly above 100 eV. Consequently, we can use the rectilinear approximation everywhere beyond 1 AU if we restrict our discussion to hydrogen ENAs with energy >400 eV. We neglect the time dependence of the proton distribution and of the neutral hydrogen density. We also make the approximation that the neutral hydrogen atoms are stationary in the observer's reference frame, because the energy of inflowing interstellar neutral atoms is $\sim$3.5 eV.

[11] There remains the issue of the kinetics of the charge exchange (and stripping) collisions between protons and hydrogen atoms. There is momentum transfer that changes the incident hydrogen's direction with a corresponding energy change of a few tens of eV. At particle energies >10 keV, the directional change is miniscule, so the ion and ENA velocity vectors are essentially identical before and after the collision. Then we can use the extreme-forward-scattering approximation with total cross-sections σ_{10} and σ_{01} for charge exchange and stripping, respectively. In this paper, we will assume that this approximation is adequate for our purposes down to energies $\sim$400 eV, because a single angular scattering of even 5° and an energy change $\sim$30 eV are not resolvable by IBEX. The heliosheath and the heliosphere beyond 1 AU are optically "thin" (mean-free-path $\sim$100 AU), and so we need only consider a single charge-exchange or stripping collision when calculating the ENA flux at 1 AU. The transport equation in this optically thin regime is well known:

$$j_{ENA}(\boldsymbol{r},\boldsymbol{u},E) = \sigma^{10}\int_0^\infty n_H(\boldsymbol{r}')j_{ion}(\boldsymbol{r}',\boldsymbol{u},E)P(\boldsymbol{r},\boldsymbol{r}')ds \qquad (2)$$

where $\boldsymbol{u} = \boldsymbol{v}/v$ is the unit vector for the ENA velocity, E is the ENA energy, n_H is the density of interstellar neutral H atoms, and s is the distance along the line of sight from the observer into the heliosheath. The unidirectional differential intensities (particles/cm^2 sr s keV) are denoted j_{ENA} for the hydrogen ENA and j_{ion} for the protons that undergo charge-exchange in the heliosheath. Loss due to re-ionization by stripping and photo-ionization is accounted for in the survival probability $P(\boldsymbol{r}, \boldsymbol{r}')$,which is a function of the observer's location, $\boldsymbol{r}$, and a point along the line of sight, $\boldsymbol{r}' = \boldsymbol{r} - \boldsymbol{u}s$, where an ENA is created. Following the analysis by *Gruntman et al.* [2001], we assume the loss rate is 6×10^{-7} s^{-1} at Earth and has a r^{-2} dependence for photo-ionization and stripping (σ_{01}).

[12] In the process of calculating the signal-to-noise ratio, we examined the count rates from the heliosheath (signal), background sources, and noise within the IBEX Hi and Lo energy sensors. Preliminary geometric factors for each sensor listed in Table 1 are based on engineering prototype tests and end-to-end simulations; final geometric factors will be available after completion of the flight sensor calibration. From the OSLG and PZO models, we calculate count rates of heliospheric ENAs on the order of 1–2 per second per IBEX energy channel. The terrestrial magnetospheric plasma sheet and ring current produce an ENA foreground on the order of 10 to 10^4 counts per second, which dominates over the heliospheric signal in those regions. Therefore counts obtained while viewing at or residing in the Earth's magnetosphere are culled from the IBEX data for the analysis of the heliospheric images.

[13] The sensors are designed to drastically reduce noise produced within the detectors by eliminating noncoincidental counts, or counts which are likely to originate from radiation rather than particles. Phenomena such as solar energetic particles may produce significantly higher count rates but can be identified with the aid of a separate energetic ion monitor provided for that purpose on IBEX–Hi. Solar energetic particle events can also be identified from other spacecraft such as ACE and STEREO.

[14] ENAs produced from the energetic tail of the cooler upstream solar wind were calculated using statistical properties of the solar wind. A worst-case scenario estimate of this flux and a comparison to the OSLG flux at the termination shock nose using a kappa distribution is given in Table 2. Using solar maximum conditions, the solar wind velocity, density, temperature, and κ number at 1 AU are assumed to be 450 km/s, 7 cm^{-3}, 150,000 K, and 1.6 respectively. The neutral hydrogen density inside the heliosphere is assumed to be 0.09 cm^{-3} as given by *Wang and Richardson* [2003] and the termination shock is assumed to be located at the Voyager 1 crossing value, 94 AU. The solar wind velocity is taken to be constant, ignoring the effect of pickup ions and disturbances, the solar wind density falls off as the inverse of the radius (r) squared, and the solar wind temperature is proportional to r$^{-0.5}$ as empirically shown up to 40 AU by *Richardson and Smith* [2003]. As this is an upper limit calculation, loss of upstream ENAs due to re-ionization is ignored. Table 2 reveals that the expected level of contamination is negligible, even in the highest IBEX channel (<14%).

[15] Maximum instrument background per energy channel is on the order of 10^{-2} counts/s, significantly lower than the average expected count rate [*McComas et al.*, 2006]. Included in this calculation are ENAs produced from charge-exchange of ions with outgassing neutrals from the

Table 2. Comparing Up and Down-Stream ENA Differential Energy Flux Estimates

Energy, keV	0.056	0.208	1.11	1.74	2.73	4.29
Upstream ENA flux, cm^{-2} s^{-1} sr^{-1} keV^{-1}	4	5	4	3	2	1
Downstream ENA flux, cm^{-2} s^{-1} sr^{-1} keV^{-1}	10^4	10^3	70	40	15	7

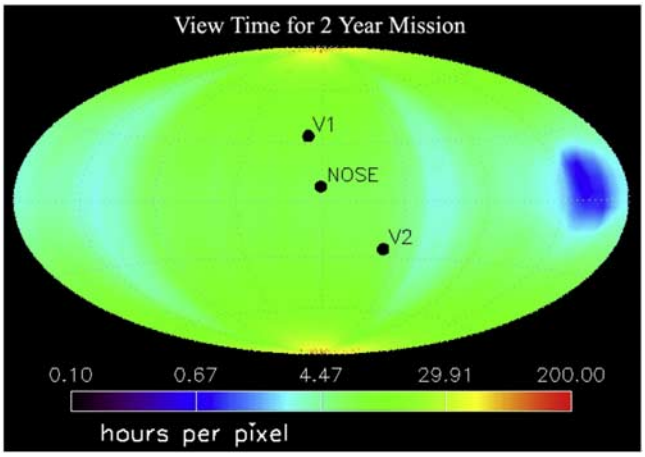

Figure 1. View time for full 2-year mission including loss of time due to magnetospheric interference show as a Hammer-Aitoff projection of the heliosphere in HSEa [*Hapgood*, 1992] coordinates. Also shown are the positions of Voyager 1, Voyager 2, and the nose of the termination shock in the MHD models. The heliospheric poles are imaged every spin and therefore get the most viewing time.

spacecraft, charge-exchange of heliospheric pickup ions with these neutrals, and secondary ions generated in the entrance subsystem. Also included are ENAs produced from CMEs, CIRs, and the magnetosheath and foreshock. Nonterrestrial planetary magnetospheres are not included in the background but are likely strong point sources of ENAs. The expected count rate for these planetary sources is unknown, but because they are localized, they are straightforward to remove from the heliospheric images. For the baseline mission lifetime of 2 years, excluding magnetospheric obstruction, viewing time for each pixel will be a minimum of 0.72 h. with an average 21 h, as shown in Figure 1. Using the OSLG model and the 2-year baseline mission duration, this corresponds to average total counts between 115 and 1282 counts/pixel/energy band. Within this same 2-year period, the maximum background is expected to be ~3 counts/pixel. Therefore Poisson noise, i.e., the square root of the number of counts, significantly dominates over other noise and background sources.

4. Results and Discussion

[16] As would be expected, the contrast between Maxwellian and kappa distributions in hydrogen ENA flux maps is significant for energies >1 keV, i.e., in the suprathermal

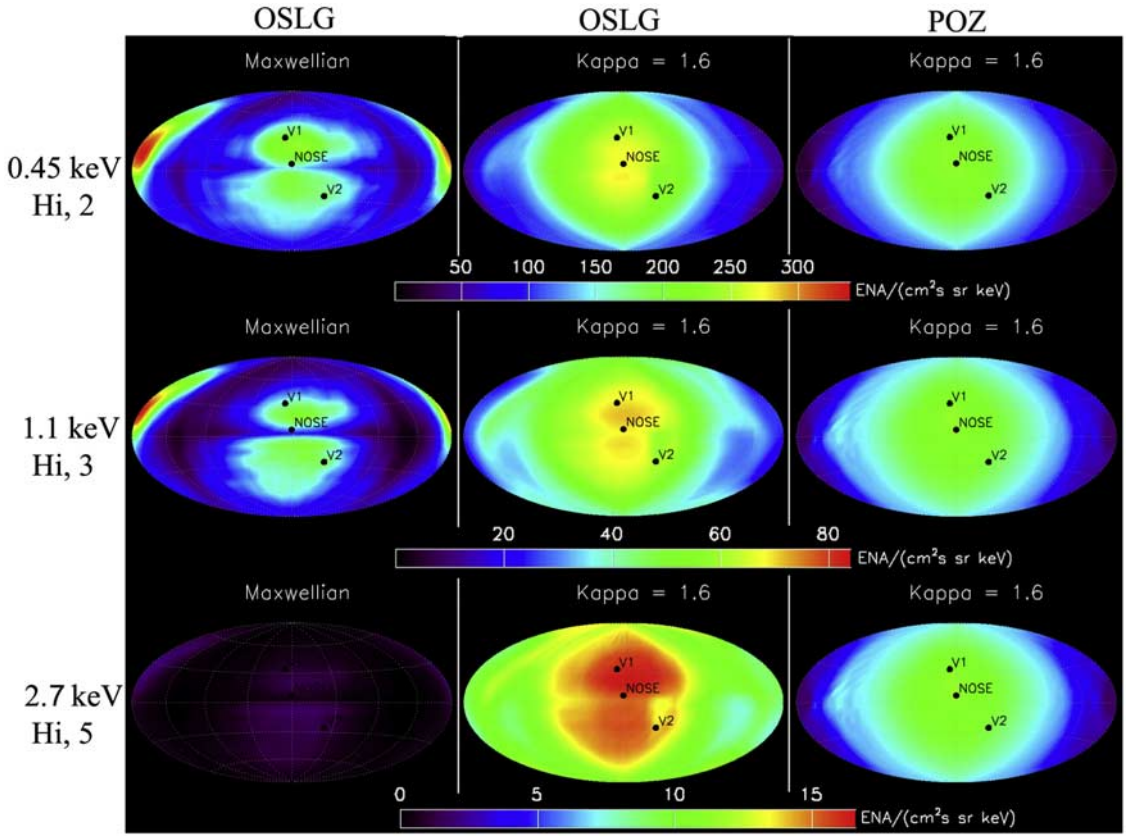

Figure 2. All-sky hydrogen ENA flux maps for several models using a Hammer-Aitoff projection in HSEa coordinates. The first two columns correspond to the OSLG model using a Maxwellian and the Voyager 1 κ value of 1.6. The third column shows the PZO model using the kappa distribution. The three rows correspond to mean energies and IBEX sensor channels 0.45 keV (Hi-2), 1.1 keV (Hi-3), and 2.7 keV (Hi-5), respectively. Also shown for reference are the positions of Voyager 1 and 2 and the nose of the TS in the MHD models.

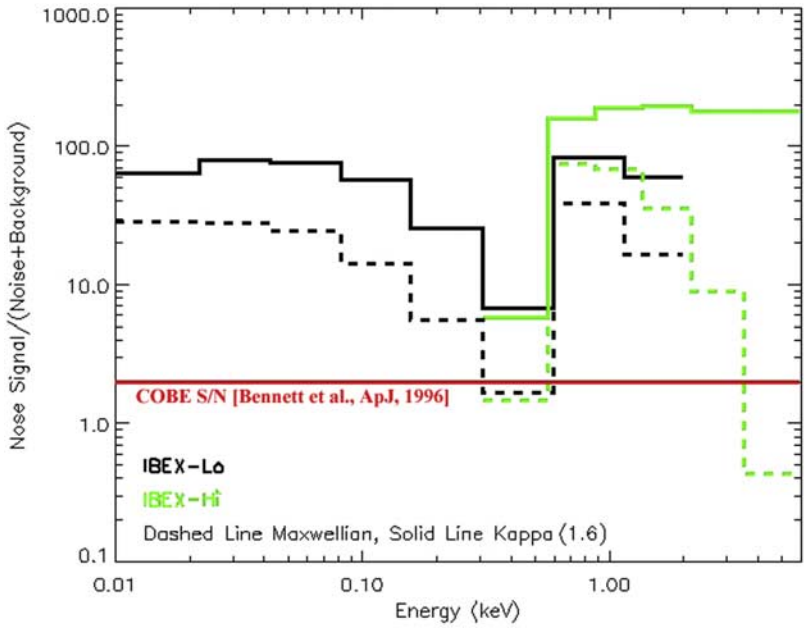

Figure 3. Signal to noise and background at the model termination shock nose for IBEX Hi (green) and IBEX Lo (black) sensors using the OSLG model for the complete two-year mission. The dashed lines correspond to a Maxwellian distribution and the solid lines are for κ of 1.6. Appearing in red is the signal to noise of 2 for the successful COBE mission [*Bennett et al.*, 1996].

tail. Figure 2 illustrates this with the ENA flux results for both the OSLG and PZO models over several energies in the IBEX range, although we show only the OSLG Maxwellian result for magnitude comparison. Above 1 keV both kappa maps have between 2 and >10 times the Maxwellian ENA flux. Closer to the thermal core the kappa and Maxwellian maps converge in intensity, again as expected. The energy transfer due to charge-exchange in the PZO heliosheath plasma produces lower proton temperature and therefore smaller ENA flux than in the OSLG model. Additional ENA fluxes, as well as temperature profiles, generated from the PZO model using a Maxwellian distribution are given by *Heerikhuisen et al.* [2007].

[17] The kappa distribution affects not only our calculations of the ENA flux but also estimates of the signal to noise due to the change in expected counts. Figure 3 shows the estimated signal to noise and background for IBEX-Hi and IBEX-Lo for both Maxwellian and kappa distributions. For the kappa distribution a larger portion of the differential flux is concentrated in upper IBEX-Hi energies and, correspondingly, the signal-to-noise ratio is improved compared to what a Maxwellian distribution produces. Shown for reference in Figure 3, the signal to noise of the successful COBE mission falls well below the expected IBEX signal to noise, reaffirming that the estimated IBEX signal to noise is high across all IBEX energy channels. Even in the lowest

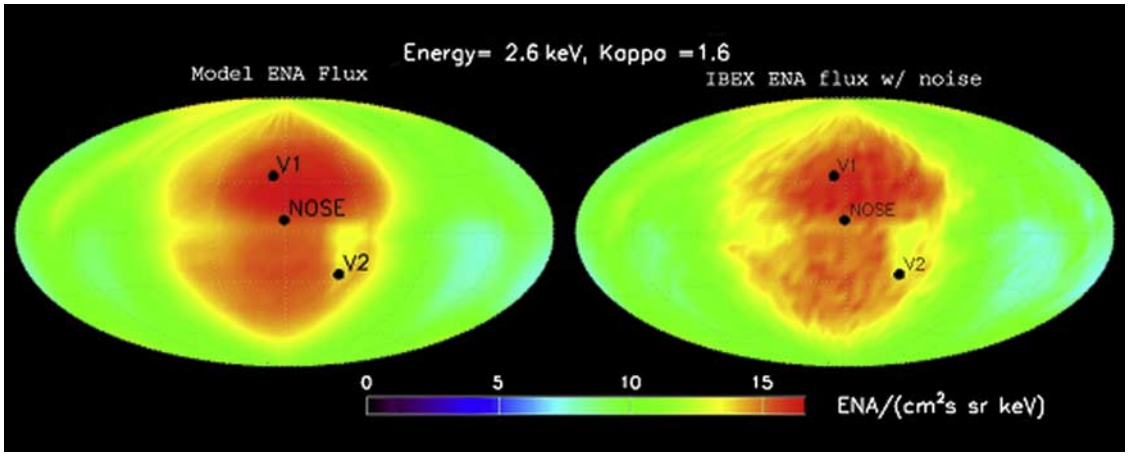

Figure 4. ENA flux for energy band 1.79 to 3.56 keV (central energy 2.6 keV) with κ = 1.6 using OSLG model. Maps are shown as a Hammer-Aitoff projection in HSEa coordinates. On the left is the original model flux and on the right is the rederived flux after processing the signal through a simulated IBEX system and including Poisson noise.

flux regime, at higher energies where the signal to noise is expected to be the worst, the global structure of ENA flux is obvious as shown in Figure 4.

5. Conclusions

[18] Proton distribution functions with power law suprathermal tails are ubiquitous in the solar wind (based on WIND, Ulysses, and ACE measurements) as well as in the heliosheath beyond the termination shock (based on Voyager 1 and Voyager 2 measurements). The kappa distribution is therefore an appropriate characterization of protons in the solar wind and the heliosheath. When we simulate ENA images that will be obtained with IBEX, we find that the kappa distribution produces significantly higher ENA fluxes than a Maxwellian does at the relevant IBEX energies. Our analysis of noise and background sources of ENAs reveals that the IBEX signal to noise is higher in all energy channels than would have been estimated using a Maxwellian distribution. When IBEX ENA images become available the simulation techniques used here will provide a starting point for inferring the global properties of suprathermal proton distributions in the heliosheath.

[19] **Acknowledgments.** This work is funded and supported by the NASA Interstellar Boundary Explorer mission, which is part of the GSFC Explorer Program. Also, the National Science Foundation Grant DGE-0221680, NASA Grant NNG06GD55G, and the NASA Heliosheath Guest Investigator Program have provided partial support for this study and are gratefully acknowledged.

[20] Wolfgang Baumjohann thanks Vytenis M. Vasyliunas and another reviewer for their assistance in evaluating this paper.

References

Bennett, C. L., et al. (1996), Four-year *COBE* DMR Cosmic Microwave Background Observations: Maps and basic results, *Astrophys. J.*, *464*, L1–L4.

Chotoo, K., et al. (2000), The suprathermal seed population for corotaing interaction region ions at 1AU deduced from composition and spectra of H^+, He^{++}, and He^+ observed by Wind, *J. Geophys. Res.*, *105*, 23,107–23,122.

Collier, M. (1995), The adiabatic transport of superthermal distributions modeled by kappa functions, *Geophys. Res. Lett.*, *22*, 2673–2676.

Collier, M. R., D. C. Hamilton, G. Gloeckler, P. Bochsler, and R. B. Sheldon (1996), Neon-20, oxygen-16, and helium-4 densities, temperatures, and suprathermal tails in the solar wind determined with WIND/MASS, *Geophys. Res. Lett.*, *23*, 1191–1194.

Decker, R. B., S. M. Krimigis, E. C. Roelof, M. E. Hill, T. P. Armstrong, G. Gloeckler, D. C. Hamilton, and L. J. Lanzerotti (2005), Voyager 1 in the foreshock, termination shock, and heliosheath, *Science*, *309*, 2020–2024.

Fisk, L. A. (1996), Implications of a weak termination shock, *Space Sci. Rev.*, *78*, 129–136.

Fisk, L. A., and G. Gloeckler (2006), The common spectrum for accelerated ions in the quiet-time solar wind, *Astrophys. J.*, *640*, L79–L82.

Gloeckler, G. (1992), The solar wind ion composition spectrometer, *Astron. Astrophys.*, *92*, 267–289.

Gloeckler, G. (2003), Ubiquitous suprathermal tails on the solar wind and pickup ion distributions, in *Solar Wind Ten: Proceedings of the Tenth International Solar Wind Conference*, edited by M. Velli, R. Bruno, and F. Malara, pp. 583–588, American Institute of Physics, New York.

Goossens, M. (2003), *An Introduction to Plasma Astrophysics and Magnetohydrodynamics*, pp. 15–88, Springer, New York.

Gruntman, M., E. Roelof, D. Mitchell, H. Fahr, H. Funsten, and D. McComas (2001), Energetic neutral atom imaging of the heliospheric boundary region, *J. Geophys. Res.*, *106*, 15,767–15,781.

Hapgood, M. A. (1992), Space physics coordinate transformations: A user guide, *Planet. Space Sci.*, *40*, 711–717.

Heerikhuisen, J., N. V. Pogorelov, G. P. Zank, and V. Florinski (2007), The effects of global heliospheric asymmetries on energetic neutral atom sky maps, *Astrophys. J.*, *655*, L53–L56.

Isenberg, P. (1997), A weaker termination shock, *Geophys. Res. Lett.*, *24*, 623–626.

McComas, D., et al. (2004), The Interstellar Boundary Explorer (IBEX), in *Physics of the Outer Heliosphere: Third International IGPP Conference*, edited by V. Florinski, N. Pogorelov, and G. Zank, pp. 162–181, American Institute of Physics, New York.

McComas, D. J., et al. (2006), The Interstellar Boundary Explorer (IBEX): Update at the end of Phase B, in *Physics of the Inner Heliosheath, CP 858, Proceedings of 5th Annual International Astrophysics Conference*, edited by J. Heerikhuisen, V. Florinski, G. Zank, and N. Pogorelov, pp. 241–250, American Institute of Physics, New York.

Opher, M., E. C. Stone, and P. Liewer (2006), The effects of a local interstellar magnetic field on Voyager 1 and 2 observations, *Astrophys. J.*, *640*, L71.

Opher, M., E. C. Stone, and T. I. Gombosi (2007), Orientation of the local interstellar magnetic field, *Science*, *16*, 875.

Pogorelov, N., G. P. Zank, and T. Ogino (2006), Three-dimensional features of the outer heliosphere due to coupling between the interstellar and interplanetary magnetic fields. Part II. The presence of neutral hydrogen atoms, *Astrophys. J.*, *644*, 1299–1316.

Richardson, J. D., and C. W. Smith (2003), The radial temperature profile of the solar wind, *Geophys. Res. Lett.*, *30*(5), 1206, doi:10.1029/2002GL016551.

Summers, D., and R. M. Thorne (1991), The modified plasma dispersion function, *Phys. Fluids*, *B3*, 1835–1847.

Treumann, R. A., et al. (1999), Generalized-Lorentzian Thermodynamics, *Phys. Scr.*, *59*, 204–214.

Treumann, R. A., C. H. Jaroschek, and M. Scholer (2004), Stationary plasma states far from equilibrium, *Phys. Fluids*, *11*, 1317–1325.

Vasyliunas, V. M. (1968), A survey of low-energy electrons in the evening sector of the magnetosphere with Ogo 1 and Ogo 3, *J. Geophys. Res.*, *73*, 2839–2884.

Wang, C., and J. D. Richardson (2003), Determination of the solar wind slowdown near solar maximum, *J. Geophys. Res.*, *108*(A2), 1058, doi:10.1029/2002JA009322.

F. Allegrini, D. J. McComas, and M. Reno, Space Science and Engineering Division, Southwest Research Institute, P.O. Drawer 28510, San Antonio, TX 78248, USA.

G. Crew, J. Passuite, C. Prested, B. Randol, N. Schwadron, and B. Stuart, Department of Astronomy, Center for Space Physics and Center for Integrated Space Weather Modeling, Boston University, 725 Commonwealth Avenue, Boston, MA 02215, USA. (cprested@bu.edu)

H. Funsten, Los Alamos National Laboratory, P.O. Box 1663, Los Alamos, NM 87545, USA.

S. Fuselier, Space Physics Laboratory, Lockheed Martin, 3251 Hanover Street, Palo Alto, CA 94304, USA.

J. Heerikhuisen, N. Pogorelov, and G. Zank, Institute of Geophysics and Planetary Physics, University of California, 900 University Way, Riverside, CA 92521, USA.

E. Moebius, Space Science Center and Department of Physics, University of New Hampshire, 39 College Road, Durham, NH 03824, USA.

M. Opher, Department of Physics and Astronomy, George Mason University, 4400 University Drive, Fairfax, VA 22030, USA.

E. Roelof, Applied Physics Laboratory, Johns Hopkins University, 11100 Johns Hopkins Road, Laurel, MD 20723, USA.

L. Saul, Physikalisches Institut, Space and Planetary Sciences, University of Bern, Sidlerstr. 5, 3012 Bern, Switzerland.